



Cite this: *Energy Environ. Sci.*, 2019, 12, 1241

Received 19th December 2018,
Accepted 7th March 2019

DOI: 10.1039/c8ee03676d

rsc.li/ees

Crystalline nickel, cobalt, and manganese antimonates as electrocatalysts for the chlorine evolution reaction†

Ivan A. Moreno-Hernandez,^a Bruce S. Brunschwig^b and Nathan S. Lewis^{b,c}

The chlorine-evolution reaction (CER) is a common, commercially valuable electrochemical reaction, and is practiced at industrial scale globally. A precious metal solid solution of RuO₂ or IrO₂ with TiO₂ is the predominant electrocatalyst for the CER. Herein we report that materials comprised only of non-precious metal elements, specifically crystalline transition-metal antimonates (TMAs) such as NiSb₂O₆, CoSb₂O₆, and MnSb₂O₆, are moderately active, stable catalysts for the electrochemical oxidation of chloride to chlorine under conditions relevant to the commercial chlor-alkali process. Specifically, CoSb₂O₆ exhibited a galvanostatic potential of 1.804 V vs. NHE at 100 mA cm⁻² of Cl₂(g) production from aqueous pH = 2.0, 4.0 M NaCl after 250 h of operation. Studies of the bulk and surface of the electrocatalyst and the composition of the electrolyte before and after electrolysis indicated minimal changes in the surface structure and intrinsic activity of CoSb₂O₆ as a result of Cl₂(g) evolution under these conditions.

Introduction

The chlor-alkali process entails the electrochemical oxidation of chloride to Cl₂(g) by the chlorine-evolution reaction (CER) in conjunction with the production of caustic soda (*i.e.*, NaOH) and H₂. The process is performed at industrial scale globally and consumes over 150 TW h of electricity annually. Dimensionally stable anodes, consisting of noble metal oxides of Ir or Ru, are the predominantly used CER anode electrocatalysts.^{1–3} The scarcity of Ir and Ru has the potential to constrain industrial use of the chlor-alkali process and limit chlorine use in applications such as water sanitation.⁴ Solid solutions of these metal oxides with TiO₂, SnO₂, CoO_x, or SbO_x have been explored to decrease

Broader context

An outstanding challenge in electrochemistry is the development of active, stable catalysts for electrochemical reactions in corrosive environments, such as oxidative reactions in low pH aqueous electrolytes. The conventional solution to this problem involves the use of noble metal oxides, but the scarcity of these materials can limit the global scalability and increase the operating costs of such electrochemical processes. The discovery of stable, active non-precious metal oxide catalysts, such as transition metal antimonates, for electrochemical reactions in such media conditions is thus important for addressing several global challenges such as water electrolysis and decentralized water sanitation.

the amount of Ir and Ru used in CER catalysts.^{5–11} The resulting RuO₂–TiO₂ anodes exhibit low corrosion rates and are operationally stable for several years. However, Ru is susceptible to the formation of thermodynamically stable species such as soluble Ru chlorides or gaseous Ru oxides, contributing eventually to catalyst degradation.^{12,13} Electrocatalysts for the CER that do not contain noble metals include Co₃O₄ and mixed first-row transition metal oxides, but these materials show limited stability under the corrosive conditions required to obtain selectivity for the CER relative to the oxygen-evolution reaction (OER).^{1,10}

Crystalline transition metal antimonates (TMAs) have recently been reported to be active and stable electrocatalysts for water oxidation in acidic electrolytes.¹⁴ Pourbaix diagrams predict that crystalline TMAs such as NiSb₂O₆, CoSb₂O₆, and MnSb₂O₆ should be stable under acidic conditions as well as in the presence of Cl₂(g).¹⁵ Accordingly, we report herein the synthesis of metal oxide films containing crystalline MSb₂O₆ (M = Ni, Co, Mn), and report the electrochemical activity and stability of these materials for the CER in acidic NaCl(aq). A primary focus is the electrochemical stability at 100 mA cm⁻² of anodic current density, due to the relevance of this current density for the commercially practiced chlor-alkali process.¹ The structural, chemical, and dissolution behaviors of crystalline MSb₂O₆ for the CER have been evaluated by scanning-electron microscopy, X-ray photoelectron spectroscopy, and inductively coupled plasma mass spectrometry.

^a Division of Chemistry and Chemical Engineering, 127-72, California Institute of Technology, Pasadena, CA 91125, USA. E-mail: nslewis@caltech.edu

^b Beckman Institute Molecular Materials Research Center, California Institute of Technology, Pasadena, CA 91125, USA

^c Kavli Nanoscience Institute, California Institute of Technology, Pasadena, CA 91125, USA

† Electronic supplementary information (ESI) available. See DOI: 10.1039/c8ee03676d

Results

Films of NiSb₂O_x, CoSb₂O_x, and MnSb₂O_x were prepared by co-sputtering Sb and M (M = Ni, Co, or Mn) onto conductive antimony-doped tin oxide (ATO) substrates.¹⁶ The catalyst loading and stoichiometry of the sputtered metallic films were determined by dissolving the films in 1.0 M H₂SO₄(aq) and measuring the amount of dissolved ions by inductively coupled plasma mass spectrometry (ICP-MS). The loading of transition metal was 375–483 nmol cm⁻² whereas the Sb loading was 709–820 nmol cm⁻², indicating a bulk M : Sb atomic ratio of ~1 : 2 (Table S1, ESI†). To obtain MSb₂O_x films, the Ni, Co, and Mn metal/Sb films were annealed at 750 °C in air.^{14,17} X-ray diffraction (XRD) data indicated that the NiSb₂O_x and CoSb₂O_x films both contained the tri-rutile MSb₂O₆ structure (Fig. S1 and S2, ESI†). MnSb₂O_x films contained MnSb₂O₆, orthorhombic Sb₂O₄, and monoclinic Sb₂O₄ (Fig. S3, ESI†). RuTiO_x films deposited on ATO and annealed at 500 °C exhibited diffraction peaks consistent with a solid solution of rutile-type RuO₂ and TiO₂ (Fig. S4, ESI†). Scanning-electron microscopy (SEM) images of the catalyst films indicated that the morphology was different for each film (Fig. S5–S8, ESI†).

The electrochemical behavior of the TMAs was evaluated by cyclic voltammetry (CV), impedance spectroscopy, and chronopotentiometry in 4.0 M NaCl(aq) that was adjusted to pH = 2 with 1.0 M HCl(aq). The equilibrium potential for Cl₂(g)/Cl⁻ was determined to be 1.331 V vs. the normal hydrogen electrode (NHE) under these experimental conditions. For comparison to the behavior of the TMA's, dimensionally stable RuTiO_x anodes were also evaluated (details in ESI†). Fig. 1a shows typical cyclic voltammograms for NiSb₂O_x, CoSb₂O_x, MnSb₂O_x, and RuTiO_x at a scan rate of 10 mV s⁻¹ in the potential range of 1.0 to 2.1 V vs. NHE. Impedance measurements yielded electrode resistances in the range of 20–200 Ω for NiSb₂O_x, CoSb₂O_x, MnSb₂O_x, and RuTiO_x films, hence compensation of 85% of the electrode resistance for electrodes with a geometric area of 0.01–0.1 cm² resulted in <30 mV of voltage compensation at current densities based on the geometric area of the electrode $j_{\text{geo}} = 10 \text{ mA cm}^{-2}$ for most of the catalysts studied herein.

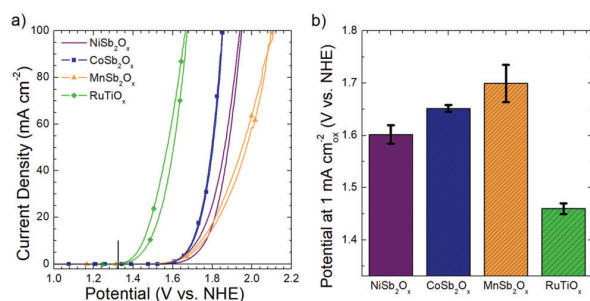


Fig. 1 Initial electrochemical behavior of NiSb₂O_x, CoSb₂O_x, MnSb₂O_x, and RuTiO_x in pH = 2.0, 4.0 M NaCl(aq) electrolyte. (a) Cyclic voltammetry of NiSb₂O_x, CoSb₂O_x, MnSb₂O_x, and RuTiO_x at a scan rate of 10 mV s⁻¹. The vertical black line indicates the thermodynamic potential for chlorine evolution in 4.0 M NaCl(aq). (b) Intrinsic potential of NiSb₂O_x, CoSb₂O_x, MnSb₂O_x, and RuTiO_x determined from cyclic voltammetry data at 1 mA cm⁻² of electrochemically active surface area.

Measurements of the electrochemically active surface area (ECSA) by impedance spectroscopy of the TMAs indicated that NiSb₂O_x, CoSb₂O_x, MnSb₂O_x, and RuTiO_x films initially had roughness factors of 1.1 ± 0.1, 6.6 ± 2.5, 9.0 ± 5.2, and 8.8 ± 3.9, respectively (Table S2, ESI†). The initial intrinsic activity of the electrocatalyst films was evaluated by determining the potential required to obtain 1 mA per cm² of ECSA from the backward scan, as shown in Fig. 1b. The potential at 1 mA cm⁻² of ECSA, which corresponds to a geometric current density of 1–15 mA cm⁻² for roughness factors of 1–15 as observed herein, is referred to as the intrinsic potential (E_i). The NiSb₂O_x, CoSb₂O_x, MnSb₂O_x, and RuTiO_x films exhibited a 1 mA cm⁻² initial intrinsic potential of 1.602 ± 0.018, 1.652 ± 0.006, 1.699 ± 0.036, and 1.460 ± 0.010 V vs. NHE, respectively (Fig. 1b and Table S3, ESI†). The initial E_i measurements thus indicated that RuTiO_x was the most active electrocatalyst at this current density, followed by NiSb₂O_x, CoSb₂O_x, and MnSb₂O_x.

Fig. 2a shows the electrochemical stability of the TMAs under galvanostatic control at $j_{\text{geo}} = 100 \text{ mA cm}^{-2}$. Cyclic voltammetry data were obtained at 1 h intervals after the chronopotentiometry data were collected (Fig. 2b). The potential increased slowly during the 1 h of chronopotentiometry with an abrupt decrease after cyclic voltammogram and impedance data were collected. High frequency transient increases in potential were also observed due to partial blockage of the catalyst film as a result of Cl₂(g) evolution. Fig. 3a shows a comparison between the potential obtained from cyclic voltammetry and chronopotentiometry at 100 mA cm⁻² after 85 h of operation for CoSb₂O_x and RuTiO_x. In general, the potential observed during extended chronopotentiometry was 10–50 mV larger than the potential determined by cyclic voltammetry.

NiSb₂O_x

For NiSb₂O_x, the potential at $j_{\text{geo}} = 100 \text{ mA cm}^{-2}$ under galvanostatic control averaged 1.874 ± 0.015 V vs. NHE during the first 30 min of operation, after which the galvanostatic potential decreased to a minimum value of 1.842 ± 0.002 V vs. NHE for 1–2 h of operation (Fig. 2a). Then the galvanostatic potential gradually increased and stabilized after 40 h, with an average value of 2.184 ± 0.022 V from 50–65 h of operation at $j_{\text{geo}} = 100 \text{ mA cm}^{-2}$ (Fig. 2a). The fluctuation in potential observed for NiSb₂O_x after 30 h was due to a periodic decrease in the potential every 5–10 min associated with bubble detachment. Impedance measurements collected after 1 h intervals of galvanostatic control indicated substantial changes in the capacitance and series resistance of the NiSb₂O_x-coated electrode. The series resistance of the NiSb₂O_x catalyst increased from 101 Ω to 165 Ω over 50 h of chronopotentiometry at $j_{\text{geo}} = 100 \text{ mA cm}^{-2}$. The increase in series resistance accounted for ~88 mV of the observed increase in potential for this film. Impedance data collected at 1 h intervals indicated that NiSb₂O_x exhibited an increase in ECSA from ~1 to ~11 after 50 h of chronopotentiometry (Fig. S9a, ESI†).

The appearance of Ni and Sb in the electrolyte was measured using ICP-MS (Fig. S10a, ESI†). After 50 h of operation, 380 nmol cm⁻² of Ni and 45 nmol cm⁻² of Sb were present

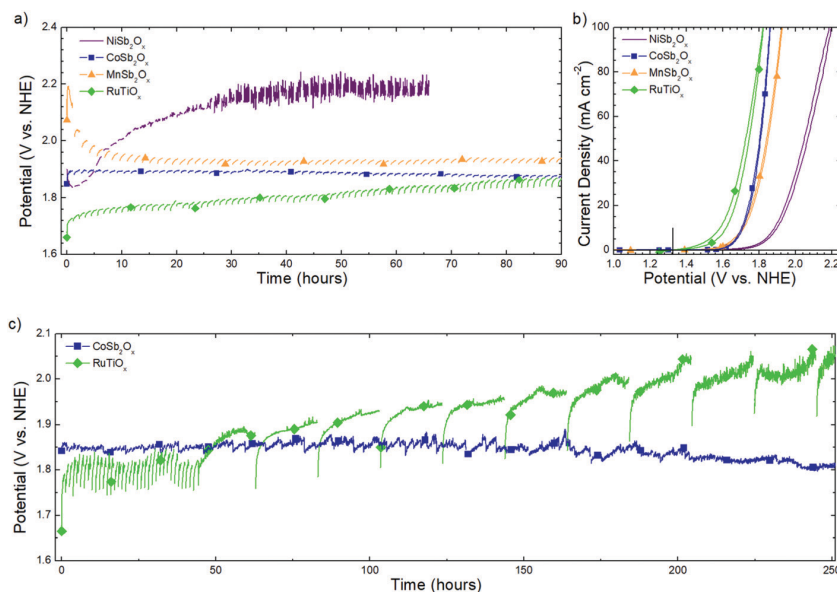


Fig. 2 (a) Chronopotentiometry of MSb_2O_x films and RuTiO_x , at $j_{\text{geo}} = 100 \text{ mA cm}^{-2}$ in 4.0 M NaCl(aq), pH = 2.0 electrolyte. (b) Cyclic voltammetry of MSb_2O_x films and of RuTiO_x , after the chronopotentiometry stability experiments, at $j_{\text{geo}} = 100 \text{ mA cm}^{-2}$ in 4.0 M NaCl(aq), pH = 2.0 electrolyte. The cyclic voltammetry data shown were recorded after operation for 65 h for NiSb_2O_x and 90 h for MnSb_2O_x , CoSb_2O_x and RuTiO_x . (c) Chronopotentiometry of CoSb_2O_x and RuTiO_x at $j_{\text{geo}} = 100 \text{ mA cm}^{-2}$ in 4.0 M NaCl(aq), pH = 2.0 electrolyte for 250 h. Cyclic voltammetry scans were collected at 1 h intervals for the first ~ 45 h, then collected at 20 h intervals from 45–250 h.

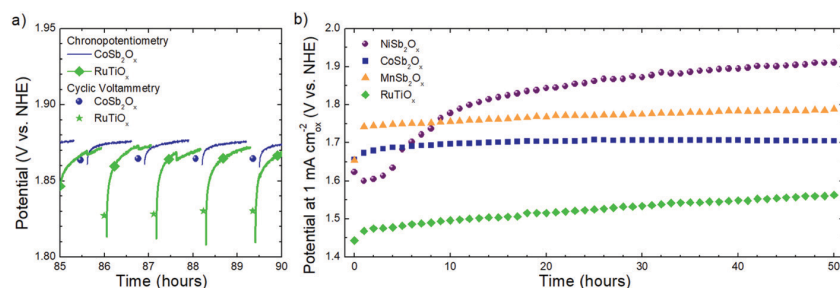


Fig. 3 (a) Comparison between potential after extended operation obtained from cyclic voltammetry and chronopotentiometry at $j_{\text{geo}} = 100 \text{ mA cm}^{-2}$ for CoSb_2O_x and RuTiO_x . (b) Intrinsic potential, E_i , at 1 mA cm^{-2} of electrochemically active surface area determined from cyclic voltammetry and impedance measurements, collected at 1 h intervals in between chronopotentiometry measurements at $j_{\text{geo}} = 100 \text{ mA cm}^{-2}$, for NiSb_2O_x , CoSb_2O_x , MnSb_2O_x , and RuTiO_x .

in the electrolyte. The detected concentration corresponded to $79 \pm 6\%$ of the Ni and $6 \pm 1\%$ of the Sb in the original catalyst film, indicating substantial loss of the catalyst layer. XRD of the electrode after electrochemical operation for 50 h indicated that crystalline NiSb_2O_6 remained in the catalyst film, and that the mean crystalline size was $39 \pm 9 \text{ nm}$ before operation and $11 \pm 1 \text{ nm}$ after operation (Fig. S1, ESI[†]). The XRD and ICP-MS data of NiSb_2O_x indicate that dissolution leads to a decrease in the mean crystalline size. SEM images indicated a loss of catalyst loading from the surface, while also indicating that the substrate remained coated with a conformal layer of catalyst (Fig. S5, ESI[†]).

CoSb_2O_x

At $j_{\text{geo}} = 100 \text{ mA cm}^{-2}$, the galvanostatic potential of CoSb_2O_x initially increased from ~ 1.851 to $\sim 1.891 \text{ V vs. NHE}$ during the first 1 h of operation, and subsequently remained at $\sim 1.876 \text{ V}$

vs. NHE after 90 h (Fig. 2a). Fig. 3a shows the comparison between the potential obtained from cyclic voltammetry and chronopotentiometry between 85–90 h of operation. The potential from cyclic voltammetry was $\sim 1.864 \text{ V vs. NHE}$, which was $\sim 12 \text{ mV}$ lower than the galvanostatic potential of $\sim 1.876 \text{ V vs. NHE}$ measured immediately preceding the cyclic voltammetry scans. Impedance measurements collected after the 1 h galvanostatic intervals indicated minor changes in the ECSA (Fig. S9b, ESI[†]). The series resistance of CoSb_2O_x remained in the range of $30\text{--}34 \Omega$ during the chronopotentiometric experiment, accounting for $< 10 \text{ mV}$ in the observed variation of the potential. The roughness factor increased from ~ 4 to ~ 8 after 50 h of operation. Less than 2 nmol cm^{-2} of Co and 3 nmol cm^{-2} of Sb dissolved into the electrolyte after 50 h of operation (Fig. S10b, ESI[†]), corresponding to a loss of $\sim 0.6 \text{ nm}$ and $\sim 0.3 \text{ nm}$ of catalyst or $0.5 \pm 0.1\%$ Co and $0.3 \pm 0.1\%$ Sb, respectively.

After electrochemical operation for 50 h, XRD data indicated that crystalline CoSb_2O_6 remained on the CoSb_2O_x catalyst film, and that the mean crystalline size was 29 ± 5 nm before operation and 41 ± 13 nm after operation (Fig. S2, ESI[†]). SEM images indicated that the morphology of CoSb_2O_x films tested for 50 h at $j_{\text{geo}} = 100 \text{ mA cm}^{-2}$ was similar to the morphology of as-synthesized films (Fig. S6, ESI[†]). Fig. 2c shows the galvanostatic potential for CoSb_2O_x at $j_{\text{geo}} = 100 \text{ mA cm}^{-2}$ for 250 h. Cyclic voltammetry data were collected at 1 h intervals for the first 45 h, then at 20 h intervals to observe the effect of long-term chronopotentiometry. The activity of CoSb_2O_x was not substantially affected by the duration between cyclic voltammetry scans. The galvanostatic potential for CoSb_2O_x at $j_{\text{geo}} = 100 \text{ mA cm}^{-2}$ was 1.804 V vs. NHE after 250 h of operation.

MnSb₂O_x

Over the first 0.3 h of operation at $j_{\text{geo}} = 100 \text{ mA cm}^{-2}$, the galvanostatic potential of MnSb_2O_x initially increased to ~ 2.191 V vs. NHE, followed by a gradual decrease to ~ 1.936 V vs. NHE over 20 h, followed by an average potential of 1.926 ± 0.006 V vs. NHE from 20 to 90 h of operation (Fig. 2a). The series resistance of the MnSb_2O_x was between 144–168 Ω during the stability test, accounting for ~ 40 mV in the observed variability in potential. The roughness factor of the MnSb_2O_x film gradually increased from ~ 3 to ~ 25 over 50 h of chronopotentiometry (Fig. S9c, ESI[†]). ICP-MS of the electrolyte indicated that 192 nmol cm^{-2} and 185 nmol cm^{-2} of Mn and Sb dissolved in the electrolyte, corresponding to $46 \pm 3\%$ of Mn and $26 \pm 1\%$ of Sb in the catalyst film (Fig. S10c, ESI[†]). After electrochemical operation, XRD confirmed that crystalline MnSb_2O_6 , monoclinic Sb_2O_4 , and orthorhombic Sb_2O_4 remained in the catalyst film, and that the mean crystalline size of MnSb_2O_x was 3.4 ± 0.1 nm before operation and 3.7 ± 0.1 nm after operation (Fig. S3, ESI[†]). After electrochemical operation, SEM images showed a loss of catalyst loading as well as an increase in film porosity (Fig. S7, ESI[†]).

RuTiO_x

Fig. 2a shows chronopotentiometry data for RuTiO_x at $j_{\text{geo}} = 100 \text{ mA cm}^{-2}$. The initial galvanostatic potential was ~ 1.661 V vs. NHE and then increased to ~ 1.871 V vs. NHE after 90 h of operation. Fig. 3a shows the comparison between the potential obtained from cyclic voltammetry and chronopotentiometry between 85–90 h of operation. The potential from cyclic voltammetry was ~ 1.828 V vs. NHE, whereas the potential was ~ 1.871 V vs. NHE from chronopotentiometry immediately preceding the cyclic voltammetry scans. The roughness factor of RuTiO_x remained essentially constant throughout the chronopotentiometry experiment (Fig. S9d, ESI[†]). The series resistance of RuTiO_x electrodes was 17–18 Ω and remained within this range for the duration of the stability test. XRD indicated that RuO_2 and TiO_2 remained in the catalyst film after electrochemical testing, and that the crystalline size was 17 ± 1 nm before operation and 25 ± 1 nm after operation (Fig. S4, ESI[†]). SEM images indicated an increase in the porosity of the RuTiO_x films after electrochemical operation (Fig. S8, ESI[†]). Fig. 2c shows the galvanostatic potential for RuTiO_x at $j_{\text{geo}} = 100 \text{ mA cm}^{-2}$ for 250 h. Cyclic voltammetry data

were collected at 1 h intervals for the first 42 h, then at 20 h intervals to observe the effect of long-term chronopotentiometry. The galvanostatic potential substantially increased during the 20 h chronopotentiometry intervals. The galvanostatic potential at $j_{\text{geo}} = 100 \text{ mA cm}^{-2}$ for RuTiO_x was 2.051 V vs. NHE after 250 h of operation.

TMA-free electrodes

To serve as controls, SbO_x on ATO and ATO electrodes were prepared without TMA electrocatalyst coatings. These electrodes exhibited a galvanostatic potential > 2.331 V vs. NHE at $j_{\text{geo}} = 100 \text{ mA cm}^{-2}$ under galvanostatic control. The electrochemical stability of the transition metal oxides NiO_x , CoO_x , and MnO_x was determined using electrocatalyst films that were prepared by the same procedure and transition-metal loading as the MSb_2O_x films, except that Sb was not co-sputtered during the metal deposition. Electrodes consisting of NiO_x or MnO_x were unstable for chlorine evolution at $j_{\text{geo}} = 100 \text{ mA cm}^{-2}$ under galvanostatic control (Fig. S11b, ESI[†]). CoO_x electrodes exhibited a potential of ~ 1.801 V vs. NHE at $j_{\text{geo}} = 100 \text{ mA cm}^{-2}$ under galvanostatic control during the first 6 h of operation, but then the potential increased to > 2.051 V vs. NHE after 8 h of operation (Fig. S11b, ESI[†]).

Intrinsic activity of the electrocatalysts

The intrinsic activity of the electrocatalyst films was obtained by calculating the intrinsic potential after 1 h intervals of galvanostatic control. After each 1 h interval of chronopotentiometry at $j_{\text{geo}} = 100 \text{ mA cm}^{-2}$, cyclic voltammetry and impedance measurements were collected to determine the ECSA, E_{cv} , series resistance, and E_i of the catalyst films. Each intrinsic potential was corrected at 85% of the series resistance determined for each time interval. Fig. 3b shows the values of E_i at 1 mA cm^{-2} of ECSA for NiSb_2O_x , CoSb_2O_x , MnSb_2O_x , and RuTiO_x obtained from these measurements. In general, the qualitative changes in both the potential (Fig. 2) and the intrinsic potential (Fig. 3b) were similar during operation for most of the electrocatalyst films. Fig. 3b shows the intrinsic potential for representative electrodes, whereas Table S3 (ESI[†]) shows the average and standard deviation for the electrocatalysts studied herein. Fig. 3b shows that NiSb_2O_x exhibited an E_i of 1.624 V vs. NHE initially, that decreased to a minimum value of 1.600 V vs. NHE after 1 h of operation and subsequently increased gradually, to 1.911 V vs. NHE after 50 h of operation. CoSb_2O_x initially exhibited an E_i of 1.656 V vs. NHE, that gradually increased to 1.704 V vs. NHE over 20 h, followed by a stable E_i of 1.704–1.707 V vs. NHE from 20 to 50 h of operation. MnSb_2O_x initially exhibited $E_i = 1.655$ V vs. NHE, that then increased to 1.741 V vs. NHE after 1 h of operation, followed by a gradual increase to $E_i = 1.789$ V vs. NHE after 50 h of operation. RuTiO_x exhibited an initial E_i of 1.443 V vs. NHE, followed by a gradual increase to 1.561 V vs. NHE after 50 h of operation. Table S3 (ESI[†]) summarizes the changes in intrinsic potential vs. time for MSb_2O_x and RuTiO_x .

Faradaic efficiency for Cl₂ production

The faradaic efficiency towards the CER was determined using iodometric titration of $\text{Cl}_2(\text{aq})$ generated at a galvanostatic

current density of 100 mA cm^{-2} . The iodometric measurements indicated that CoSb_2O_x had the highest faradaic efficiency for the CER ($97.4 \pm 3.0\%$), with NiSb_2O_x ($96.0 \pm 3.7\%$), RuTiO_x ($94.8 \pm 0.9\%$), and MnSb_2O_x ($89.9 \pm 0.8\%$) having a slightly lower faradaic efficiency towards the CER but still predominantly evolving $\text{Cl}_2(\text{g})$ preferentially relative to oxidizing water (Table S2, ESI†). The production of chlorine was also confirmed with colorimetric measurements using *N,N*-diethyl-*p*-phenylenediamine. Cyclic voltammograms collected in $\text{pH} = 2.0 \text{ H}_2\text{SO}_4(\text{aq})$, with current solely attributable to the OER, further confirmed minimal activity towards the OER for CoSb_2O_x in the potential range relevant to the CER (Fig. S13, ESI†).

Surface composition as probed by XPS

Fig. 4 shows high-resolution XP spectra of NiSb_2O_x , CoSb_2O_x , and MnSb_2O_x before and after chronopotentiometry at $j_{\text{geo}} = 100 \text{ mA cm}^{-2}$. The Ni 2p spectra of NiSb_2O_x exhibited a peak at $\sim 856.1 \text{ eV}$. The peak shapes of NiSb_2O_x were fitted to two Ni(II) components, $\text{Ni}(\text{OH})_2$ and a peak shape similar to $\text{Ni}(\text{OH})_2$ but with a 1.0 eV more positive binding energy. The observed binding energy for the more positive contribution is intermediate to that of Ni(II) in NiCl_2 and $\text{Ni}(\text{OH})_2$.¹⁸ In general, the M 2p spectra of TMAs exhibited peak shapes similar to that of the $\text{M}(\text{OH})_2$ or MO species, but with more positive binding energies. NiSb_2O_6 is chemically different than Ni oxides and hydroxides, so the Ni 2p peak binding energy can be different while remaining in the 2+ oxidation state. Thus, we assign the more positive contribution to Ni(II) in the NiSb_2O_6 lattice. After electrochemical operation, NiSb_2O_x samples exhibited a narrower Ni 2p_{3/2} peak at $856.3 \pm 0.1 \text{ eV}$ compared to NiSb_2O_x before electrochemical operation. The peak shape of NiSb_2O_x after electrochemical operation could be adequately fit with a peak shape similar to $\text{Ni}(\text{OH})_2$ but shifted positively by 1.0 eV. XP spectra in the Cl, Ir, and Ru

regions revealed no detectable Cl, Ir, and Ru before or after electrochemical operation. Mutually similar Sb 3d_{3/2} binding energies were observed for NiSb_2O_x before ($540.4 \pm 0.1 \text{ eV}$) and after ($540.5 \pm 0.1 \text{ eV}$) electrochemical operation. The Sb binding energy is consistent with the samples containing Sb^{5+} as well as minor contributions from Sb^{3+} .¹⁹ The surface stoichiometry of the NiSb_2O_x was $1:1.8 \pm 0.1 \text{ Ni:Sb}$ prior to electrochemical operation and was $1:3.2 \pm 0.1 \text{ Ni:Sb}$ after electrochemical operation, indicating that the surface became Sb rich. The catalyst surface coverage was determined by comparing the catalyst metal signal (Ni + Sb) to the overall metal signal of the catalyst and the substrate (Ni + Sb + Sn), with the signals corrected using the respective relative sensitivity factors. The catalyst coverage was 100% of the surface in both cases.

Before and after electrochemical operation, CoSb_2O_x samples exhibited a narrow Co 2p_{3/2} XPS peak at $781.2 \pm 0.1 \text{ eV}$. The peak shape of Co in CoSb_2O_x was similar to that of Co in $\text{Co}(\text{OH})_2$, but with a $\sim 0.5 \text{ eV}$ higher binding energy.²⁰ The observed binding energy is between that of hydrated CoCl_2 and $\text{Co}(\text{OH})_2$, indicating that Co is in the 2+ oxidation state at the surface of the CoSb_2O_x films.²⁰ The XPS measurements indicate that the oxidation state of Co did not irreversibly change as a result of electrochemical operation. Wide scan XP spectra showed no detectable Cl, Ir, or Ru on the electrodes. The Sb 3d_{3/2} binding energy was $540.6 \pm 0.1 \text{ eV}$ prior to electrochemical operation and $540.3 \pm 0.1 \text{ eV}$ after electrochemical operation. The XPS measurements indicate that Sb was present in the 5+ oxidation state prior to electrochemical operation and was in a mixed 5+/3+ oxidation state after electrochemical operation.¹⁹ The surface stoichiometry of CoSb_2O_x was $1:4.0 \pm 0.1 \text{ Co:Sb}$ prior to electrochemical operation and was $1:4.5 \pm 0.1 \text{ Co:Sb}$ after electrochemical operation, indicating enrichment of Sb at the surface. The CoSb_2O_x surface catalyst coverage was 100% before and after electrochemical operation.

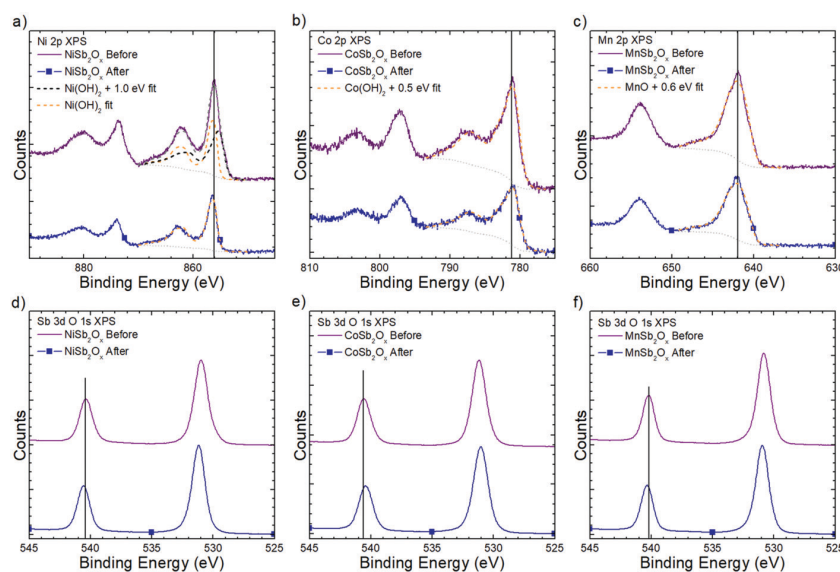


Fig. 4 X-ray photoelectron spectra of TMAs before and after electrochemical operation: (a) NiSb_2O_x Ni 2p spectra, (b) CoSb_2O_x Co 2p spectra, (c) MnSb_2O_x Mn 2p spectra, and Sb 3d and O 1s spectra of (d) NiSb_2O_x , (e) CoSb_2O_x , and (f) MnSb_2O_x .

The MnSb_2O_x samples exhibited a Mn $2p_{3/2}$ XPS peak at a binding energy of 641.9 ± 0.1 eV before electrochemical operation and 642.0 ± 0.1 eV after electrochemical operation. The binding energies are comparable to Mn in the 2+ oxidation state in MnCl_2 , and the peak shape was similar to MnO but shifted 0.5 eV more positive.^{20,21} Wide scan XP spectra indicated no detectable Cl, Ir, or Ru on the surface. The Sb $3d_{3/2}$ peak exhibited a binding energy of 540.2 ± 0.1 eV prior to electrochemical operation and 540.3 ± 0.1 eV after electrochemical operation. The Sb 3d spectra indicated that Sb was present in both the 5+ and 3+ oxidation states before and after electrochemical operation. The surface stoichiometry of MnSb_2O_x was $1:2.0 \pm 0.1$ Mn:Sb prior to electrochemical operation and $1:2.7 \pm 0.2$ Mn:Sb after electrochemical operation, indicating surface enrichment of Sb after chlorine evolution. The surface coverage of MnSb_2O_x was $98.8 \pm 0.4\%$ prior to electrochemical operation and $96.8 \pm 0.1\%$ after electrochemical operation, indicating partial exposure of the electrocatalyst substrate after chlorine evolution. Table S4 (ESI[†]) summarizes the observed binding energies of the MSb_2O_x samples and also presents a comparison of the binding energies to literature values. Fig. S14 (ESI[†]) summarizes the roughness factor, potential, stoichiometry, and crystalline size of the catalysts studied herein after different durations of galvanostatic operation.

Discussion

Trends in catalyst intrinsic activity

The initial intrinsic activity measurements of TMAs under chlorine evolution indicate an activity trend of $\text{NiSb}_2\text{O}_x > \text{CoSb}_2\text{O}_x > \text{MnSb}_2\text{O}_x$. Previous studies of the intrinsic OER activity of MSb_2O_x in acidic electrolytes indicated an OER activity trend of $\text{NiSb}_2\text{O}_x \approx \text{MnSb}_2\text{O}_x$, while CoSb_2O_x was not previously examined for the OER.¹⁴ Further improvements in the activity of TMAs towards chlorine evolution could possibly be achieved *via* solid solutions, as has been demonstrated for OER electrocatalysts and/or by use of other transition metals in the SbO_x framework.¹⁴ Notably, CoSb_2O_x had the highest CER activity after extended operation (Fig. 2 and Fig. S13, ESI[†]). While the CoSb_2O_x catalyst had an initial intrinsic potential that was ~ 190 mV higher than RuTiO_x , this difference decreased to ~ 140 mV after 50 h of chronopotentiometry, due to the intrinsic potential of RuTiO_x increasing (~ 1.3 mV h^{-1}) while the CoSb_2O_x intrinsic potential remained constant after an initial increase (Fig. 3b). The high stability of the electrochemical activity of CoSb_2O_x relative to RuTiO_x suggests that CoSb_2O_x electrodes could have active electrocatalytic CER lifetimes exceeding those of RuTiO_x .

During chlorine evolution, the surface composition of the TMAs changed, and correlated with changes in the intrinsic activity of the catalyst films. As indicated by XPS, NiSb_2O_x and MnSb_2O_x exhibited surface compositions that were very similar to their bulk composition ($\sim 1:2$ M:Sb), but CoSb_2O_x exhibited substantial initial surface enrichment of Sb (1:4 Co:Sb) despite having a bulk composition of $\sim 1:2$ M:Sb (Fig. 4 and Table S1, ESI[†]). The surface enrichment of CoSb_2O_x is consistent with previous reports for cobalt antimony oxides.²²

The intrinsic potential of NiSb_2O_x films initially decreased by 32 mV during operation, followed by an increase of 300 mV (Fig. 3). While the Ni 2p spectra indicate that Ni is in the 2+ oxidation state before and after electrochemical operation, Ni(II) compounds such as NiO, Ni(OH)_2 , NiCl_2 , and NiSb_2O_6 have different peak binding energies despite having the same formal oxidation state. Fitting of the Ni 2p peak shape can reveal which species are present on the surface.²³ The spectrum of NiSb_2O_x could not be adequately fit with the fitting parameters of previously reported species, so NiSb_2O_x was fit by using the peak shape of Ni(OH)_2 shifted positively by 1.0 eV. The observed contributions at 1.0 eV more positive binding energies could correspond to Ni(II) in the NiSb_2O_6 lattice. Fitting the Ni 2p data of NiSb_2O_x before electrochemical operation with the proposed NiSb_2O_6 fit revealed low binding energy contributions that are consistent with Ni hydroxide species (Fig. 4a). The surface composition of the NiSb_2O_x was similar to its bulk composition ($\sim 1:2$ M:Sb), but the XPS data suggest that the surface was covered by multiple Ni(II) species, such as NiSb_2O_6 , NiO_x , and Ni(OH)_2 (Fig. 4a). NiO_x and Ni(OH)_2 are expected to be readily removed from the surface due to thermodynamically favored dissolution processes under the operating conditions, and NiO_x is unstable towards the CER (Fig. S11b, ESI[†]). Loss of NiO_x and Ni(OH)_2 in the first hour of operation could explain the initial improvement in catalytic activity, if these species had a detrimental effect on the activity. After 50 h of operation, NiSb_2O_x exhibited substantial surface enrichment of Sb, as indicated by the $\sim 80\%$ increase of Sb relative to Ni (Fig. 4a and d). The Ni in NiSb_2O_x exhibited a 2+ oxidation state before and after electrochemical operation. Contributions from Ni(OH)_2 or NiO_x decreased after electrochemical operation as indicated by the Ni 2p XPS data, suggesting that the surface Ni either dissolved or is in a NiSb_2O_6 lattice and did not undergo conversion to stable Ni oxides or (oxy)hydroxides.

The intrinsic potential of MnSb_2O_x increased by ~ 85 mV in the first hour of operation but increased by only another 20 mV in the next 50 h. The oxidation states of both Mn and Sb did not change substantially after electrochemical operation (Fig. 4b and e). However, the surface of the MnSb_2O_x became Sb rich, as indicated by the $\sim 39\%$ increase in Sb at the surface compared to Mn as measured by XPS. The increase in Sb at the surface, without a substantial change in binding energy, suggests that Sb remained in the 5+ oxidation state. The substantially smaller change in potential after 50 h for MnSb_2O_x ($\Delta E_i = 134$ mV) as compared to NiSb_2O_x ($\Delta E_i = 287$ mV) might be due to a lower surface coverage of SbO_x species (Fig. 3 and 4).

The surface of CoSb_2O_x differed substantially from the surface of NiSb_2O_x or MnSb_2O_x . CoSb_2O_x exhibited substantial initial surface enrichment of Sb (1:4 Co:Sb) prior to electrochemical operation in contrast to both NiSb_2O_x and MnSb_2O_x that had an initial surface M:Sb ratio close to their bulk stoichiometry of $\sim 1:2$. The CoSb_2O_x exhibited an increase in surface Sb (1:4.5 Co:Sb) after electrochemical operation ($\sim 13\%$), again in contrast to NiSb_2O_x and MnSb_2O_x whose Sb surface enrichment after electrochemical operation increased $\sim 80\%$, and $\sim 39\%$, respectively. However, in all cases after electrochemical operation

the surfaces were substantially enriched in Sb relative to the transition metal. As opposed to the NiSb_2O_x and MnSb_2O_x electrodes, the CoSb_2O_x electrode exhibited a minimal change in intrinsic potential after 50 h ($\Delta E_i = 48$ mV), which correlates with the minimal change in Sb enrichment at the surface. The initial oxidation states of Co and Sb at the surface were 2+ and 5+, in accord with expectations for stoichiometric CoSb_2O_6 (Fig. 4). After electrochemical testing, CoSb_2O_x exhibited a decrease of 0.3 eV in Sb $3d_{5/2}$ binding energy, whereas NiSb_2O_x and MnSb_2O_x both exhibited an increase in the binding energy of Sb $3d_{5/2}$ ($\Delta E = 0.1$ eV). The decrease in binding energy of Sb in CoSb_2O_x could be related to the Sb-rich layer on the surface of CoSb_2O_x , which is not present in the nearly stoichiometric surface of the NiSb_2O_x and MnSb_2O_x films before electrochemical operation. Cyclic voltammetry data were collected at more negative potentials than the thermodynamic potential for chlorine evolution, and cathodic current was observed at such potentials (Fig. 2b). Further studies to determine the catalytically active site of TMAs could allow more detailed elucidation of the electrocatalytic role of the Sb oxidation state.

Comparison of activity to other CER electrocatalysts

Previous studies of chlorine evolution catalysts have included Co_3O_4 , which exhibits ~ 1.951 V vs. NHE at $j_{\text{geo}} = 100$ mA cm^{-2} , with an estimated catalyst roughness factor of > 3000 .²⁴ Nanostructured RuO_2 - TiO_2 electrodes exhibit ~ 2.041 V vs. NHE at $j_{\text{geo}} = 250$ mA cm^{-2} , with an estimated roughness factor of ~ 390 .²⁵ $\text{Ir}_{0.7}\text{Ta}_{0.3}\text{O}_y$ films exhibit > 2.331 V vs. NHE at $j_{\text{geo}} = 30$ mA cm^{-2} in pH = 7, 50 mM NaCl(aq) electrolyte.²⁶ Mesoporous Ru/ TiO_2 dimensionally stable anodes exhibit ~ 1.981 V vs. NHE at $j_{\text{geo}} = 100$ mA cm^{-2} in 4.0 M NaCl(aq), pH = 3.0 electrolyte.⁸ The ~ 1.871 V vs. NHE galvanostatic potential at $j_{\text{geo}} = 100$ mA cm^{-2} reported herein for RuTiO_x between 85 – 90 h of operation is comparable to previous reports of noble metal oxides for chlorine evolution (Fig. 2a). CoSb_2O_x exhibits a galvanostatic potential of ~ 1.804 V vs. NHE at $j_{\text{geo}} = 100$ mA cm^{-2} after 250 h, which is lower than some previous reports for noble metal oxides and is lower than the potential observed herein for RuTiO_x after extended operation (Fig. 2c). The catalyst loading and roughness factor used herein were both relatively low, to facilitate determination of the intrinsic properties of the electrocatalysts. Consequently, the potential of the TMAs could be improved further by increasing the catalyst loading and roughness, to expose additional catalytically active sites without changing the geometric area of the electrode. Due to the deactivation of RuTiO_x during chronopotentiometry and the comparatively high electrochemical stability of CoSb_2O_x , after 250 h of operation at $j_{\text{geo}} = 100$ mA cm^{-2} CoSb_2O_x exhibited a galvanostatic potential ~ 247 mV lower than that of RuTiO_x (~ 2.051 V vs. NHE). This behavior suggests that CoSb_2O_x may constitute a promising alternative to RuTiO_x for the chlor-alkali process and other processes that require the CER. Co and Sb are substantially more abundant than Ru, and their annual molar production rates are over 5000 times higher than Ru.²⁷ The high abundance of both Co and Sb relative to Ru is reflected in the market price of these elements, which reflects a substantially

lower price per mole of metals for CoSb_2O_x (~ 2 USD mol^{-1}) compared to the price per mol for the commercially used $\text{Ru}_{0.3}\text{Ti}_{0.7}\text{O}_x$ (~ 153 USD mol^{-1}) catalyst.²⁷

Trends in catalyst stability

Under CER conditions, the chemical stability of the TMA's decreased in the order $\text{CoSb}_2\text{O}_x > \text{MnSb}_2\text{O}_x > \text{NiSb}_2\text{O}_x$. CoSb_2O_x exhibited the lowest dissolution rate, with < 0.6 nm of Co (~ 2 nmol cm^{-2}) and < 0.3 nm of Sb lost (~ 3 nmol cm^{-2}) from the surface after 50 h of operation (Fig. S10b, ESI[†]). Possible explanations for the appearance of M and Sb in the electrolyte include dissolution of oxide species that did not form the stable MSb_2O_6 phase, and/or chemically or electrochemically driven dissolution processes. Additionally, mechanical detachment of MSb_2O_6 particles could lead to changes in the catalyst loading that cannot be detected with ICP-MS. The small amount of dissolved Co and Sb ($\sim 4 \times 10^{-9}$ mol cm^{-2}) for CoSb_2O_x , compared to the charge passed during the stability experiments ($\sim 1.8 \times 10^4$ C cm^{-2}), suggests a turnover number of $> 2 \times 10^7$ based on the dissolution observed per charge passed, indicating that faradaic dissolution pathways are unlikely to be dominant. After 250 h at $j_{\text{geo}} = 100$ mA cm^{-2} , the CoSb_2O_x electrocatalyst has thus turned-over $\sim 10^6$ equivalents of Cl_2 without substantial degradation. While the dissolution studies indicate that CoSb_2O_x has high electrochemical stability, industrial applications will require toxicology studies to determine possible exposure routes to Co and Sb. Similar studies have been conducted for polyethylene terephthalate bottles used for water consumption containing an antimony trioxide polymerization catalyst.²⁸ The high turnover number suggest that Sb could be present at ~ 0.05 ppm concentrations in the products of the chlor-alkali process utilizing a CoSb_2O_x electrocatalysts. However, since chlorine is usually used in the 1–3 ppm range to disinfect water, the dilution of chlorine would also lead to the dilution of Sb, which could lead to an Sb concentration of ~ 0.15 parts-per-trillion. Antimony is limited to 5–6 ppb in drinkable water in the United States and the European Union, which is $\sim 3 \times 10^4$ greater than the concentration expected for water treated with diluted chlorine generated with a CoSb_2O_x catalyst under the specific experimental conditions evaluated in this work. The high chemical and electrochemical stability of CoSb_2O_x , as indicated by minimal changes in catalyst morphology, intrinsic potential, and surface oxidation, suggest that CoSb_2O_x and possibly other TMAs could be viable materials for chlorine evolution in devices requiring abundant and stable electrocatalysts under industrially relevant operational conditions.

Conclusion

NiSb_2O_x , CoSb_2O_x , and MnSb_2O_x were found to be moderately active chlorine evolution catalysts for > 60 h at $j_{\text{geo}} = 100$ mA cm^{-2} in 4.0 M NaCl(aq), pH = 2.0 electrolyte. CoSb_2O_x exhibited the highest stability and selectivity among the TMAs tested herein, with < 1 nm of metals lost after extended electrochemical operation. After 250 h of operation, the galvanostatic potential of CoSb_2O_x at $j_{\text{geo}} = 100$ mA cm^{-2} was lower than that

of dimensionally stable RuTiO_x. The results suggest that TMAs could be further modified to potentially yield stable catalysts for chlorine evolution with lifetimes and selectivity comparable to or greater than that of dimensionally stable anodes such as RuTiO_x.

Conflicts of interest

There are no conflicts to declare.

Acknowledgements

This work was supported through the Office of Science of the U.S. Department of Energy (DOE) under award no. DE-SC0004993 to the Joint Center for Artificial Photosynthesis, a DOE Energy Innovation Hub. I. A. M.-H. acknowledges a National Science Foundation Graduate Research Fellowship under Grant No. DGE-1144469. We thank Dr K. Papadantonakis for assistance with editing the manuscript, and C. Finke for assistance with iodometric measurements.

References

- R. K. Karlsson and A. Cornell, *Chem. Rev.*, 2016, **116**, 2982–3028.
- H. A. Hansen, I. C. Man, F. Studt, F. Abild-Pedersen, T. Bligaard and J. Rossmeisl, *Phys. Chem. Chem. Phys.*, 2010, **12**, 283–290.
- K. S. Exner, J. Anton, T. Jacob and H. Over, *Angew. Chem., Int. Ed.*, 2014, **53**, 11032–11035.
- C. A. Martinez-Huitle and S. Ferro, *Chem. Soc. Rev.*, 2006, **35**, 1324–1340.
- L. Nanni, S. Polizzi, A. Benedetti and A. D. Battisti, *J. Electrochem. Soc.*, 1999, **146**, 220–225.
- R. K. B. Karlsson, H. A. Hansen, T. Bligaard, A. Cornell and L. G. M. Pettersson, *Electrochim. Acta*, 2014, **146**, 733–740.
- K. Xiong, Z. Deng, L. Li, S. Chen, M. Xia, L. Zhang, X. Qi, W. Ding, S. Tan and Z. Wei, *J. Appl. Electrochem.*, 2013, **43**, 847–854.
- N. Menzel, E. Ortel, K. Mette, R. Kraehnert and P. Strasser, *ACS Catal.*, 2013, **3**, 1324–1333.
- H. Cao, D. Lu, J. Lin, Q. Ye, J. Wu and G. Zheng, *Electrochim. Acta*, 2013, **91**, 234–239.
- S. Trasatti, *Electrochim. Acta*, 1984, **29**, 1503–1512.
- A. R. Zeradjanin, N. Menzel, W. Schuhmann and P. Strasser, *Phys. Chem. Chem. Phys.*, 2014, **16**, 13741–13747.
- T. Loucka, *J. Appl. Electrochem.*, 1990, **20**, 522–523.
- H. B. Beer, *US Pat.*, 4052271, 1977.
- I. A. Moreno-Hernandez, C. A. MacFarland, C. G. Read, K. M. Papadantonakis, B. S. Brunshwig and N. S. Lewis, *Energy Environ. Sci.*, 2017, **10**, 2103–2108.
- A. Jain, S. P. Ong, G. Hautier, W. Chen, W. D. Richards, S. Dacek, S. Cholia, D. Gunter, D. Skinner, G. Ceder and K. A. Persson, *APL Mater.*, 2013, **1**, 011002.
- H. Bisht, H.-T. Eun, A. Mehrrens and M. A. Aegerter, *Thin Solid Films*, 1999, **351**, 109–114.
- G. Westin and M. Nygren, *J. Mater. Chem.*, 1993, **3**, 367–371.
- M. C. Biesinger, L. W. Lau, A. R. Gerson and R. S. Smart, *Phys. Chem. Chem. Phys.*, 2012, **14**, 2434–2442.
- R. Izquierdo, E. Sacher and A. Yelon, *Appl. Surf. Sci.*, 1989, **40**, 175–177.
- M. C. Biesinger, B. P. Payne, A. P. Grosvenor, L. W. M. Lau, A. R. Gerson and R. S. C. Smart, *Appl. Surf. Sci.*, 2011, **257**, 2717–2730.
- A. Aoki, *Jpn. J. Appl. Phys.*, 1976, **15**, 305–311.
- G. I. Straguzzi, K. B. Bischoff, T. A. Koch and G. C. A. Schuit, *J. Catal.*, 1987, **103**, 357–365.
- M. C. Biesinger, B. P. Payne, L. W. M. Lau, A. Gerson and R. S. C. Smart, *Surf. Interface Anal.*, 2009, **41**, 324–332.
- X. Zhu, P. Wang, Z. Wang, Y. Liu, Z. Zheng, Q. Zhang, X. Zhang, Y. Dai, M. Whangbo and B. Huang, *J. Mater. Chem. A*, 2018, **6**, 12718–12723.
- M. Jiang, H. Wang, Y. Li, H. Zhang, G. Zhang, Z. Lu, X. Sun and L. Jiang, *Small*, 2017, **13**, 1602240.
- K. Cho and M. R. Hoffmann, *Chem. Mater.*, 2015, **27**, 2224–2233.
- P. C. K. Vesborg and T. F. Jaramillo, *RSC Adv.*, 2012, **2**, 7933.
- E. M. Aghaee, M. Alimohammadi, R. Nabizadeh, G. J. Khaniki, S. Naseri, A. H. Mahvi, K. Yaghmaeian, H. Aslani, S. Nazmara, B. Mahmoudi and M. Ghani, *J. Environ. Health Sci. Eng.*, 2014, **12**, 133.